

On the Practical Design of a Two-Terminal Active Capacitor

Haoran Wang , *Member, IEEE*, Yang Liu , *Senior Member, IEEE*, and Huai Wang , *Senior Member, IEEE*

Abstract—A two-terminal active capacitor concept has been proposed recently based on an active power electronic circuit with a voltage control method and self-power scheme. It retains the convenience of use as a passive capacitor with two power terminals only without any additional required connections and has the potential to either increase power density or reduce design cost depending on the applications. Based on the previously proof-of-concept study, this paper addresses the design constraints, impedance modeling, and start-up solutions of two-terminal active capacitors. A design method for functionality, efficiency, lifetime, and cost-constraint applications is applied to size the active components and passive elements. A voltage feedforward control scheme is implemented to improve its dynamic response. Two start-up solutions are proposed to overcome the issues brought by the self-power scheme. A case study of an active capacitor for the dc link of a single-phase full-bridge rectifier is presented to demonstrate the theoretical analyses.

Index Terms—Active circuits, capacitors, power converter, reliability.

I. INTRODUCTION

THE applications of power electronics consume unprecedented quantities of capacitors for harmonic filtering, power balancing, and/or short-term energy storage. In a single-phase voltage-source rectifier or inverter system, the capacitive dc link needs to filter low-frequency current components while limiting the voltage variation within a specific range. In a three-phase system, possible unbalances appearing in line voltages and/or loads introduce low-frequency harmonics in the dc link [1]. Therefore, a bulky capacitor bank is required for the capacitive dc links in most single-phase and three-phase applications. Moreover, large capacitor banks are also necessary for the ac filters in MW-level high-power inverter applications [2].

Manuscript received October 24, 2018; revised December 7, 2018; accepted January 5, 2019. Date of publication January 15, 2019; date of current version June 28, 2019. This work was supported in part by the Innovation Fund Denmark through the Advanced Power Electronic Technology and Tools Project, and in part by the Funds for International Cooperation and Exchange of Dongguan, Guangdong Province, China under Grant 2016508102005. Recommended for publication by Associate Editor K. Ngo. This paper was presented in part at the IEEE International Symposium on Diagnostics for Electric Machines, Power Electronics and Drives, Tinos, Greece, August/September 2017, and the 18th IEEE Workshop on Control and Modeling for Power Electronics, Stanford, CA, USA, July 2017. (*Corresponding author: Huai Wang.*)

H. Wang and H. Wang are with the Department of Energy Technology, Aalborg University, Aalborg 9220, Denmark (e-mail:

active capacitor design as well. Therefore, the focus of the following discussions is on cost-constraint applications, which is relevant to most industry sectors. The practical challenge for this type of applications is to design the active capacitors to fulfill the functionality, efficiency, and lifetime target with minimum cost. Such component sizing procedure is presented in [13] based on the reliability-oriented design method [14] [15] and power electronic component cost models discussed in [16]–[18]. For dynamic response and impedance characteristic analyses, the large-signal modeling and small-signal modeling are widely applied tools [19]. Voltage feedforward control is one of the solutions to improve dynamic response and voltage stabilization [20], [21], which is also worthwhile exploring for the two-terminal active capacitors. Different start-up circuits [22]–[24] or start-up algorithms [25], [26] are applied in practical designs to limit the inrush current of power electronic converters. Nevertheless, these start-up methods cannot be directly applied for the two-terminal active capacitors due to the following reasons.

- 1) The active capacitors do not have an internal power source for its gate drivers and controllers during the startup.
- 2) Its components have relatively low voltage ratings with limited over-voltage capability.

This paper aims to propose associated methods to overcome the above-mentioned three aspects of practical design challenges of the two-terminal active capacitors for cost-constraint applications. Besides the analysis of design constraints, the study on dynamic response and impedance characteristics modeling, and start-up solutions is also applicable for high power density applications. Even though parts of the results to be discussed in this paper have already been presented in previous conference publications [27], [28], it is worthwhile having a more comprehensive discussions on all the three important aspects by one case study. Moreover, new results are added including the following.

- 1) Theoretical analysis and mathematical model for the impedance characteristics of the active capacitor are presented in this paper.
- 2) Investigation of a start-up issue and corresponding solutions, including component sizing and start-up circuit.

The structure of this paper is as follows. Section II briefly introduces the two-terminal active capacitor concept. Section III discusses the design constraints and component sizing procedure of the active capacitors in terms of electrical performance, cost, and reliability. Section IV presents the impedance characteristic modeling of the active capacitors with and without feedforward control scheme. Section V gives the start-up procedure analysis and proposes two start-up solutions for the active capacitors. Section VI demonstrates a case study of a two-terminal active capacitors for a single-phase capacitive dc-link application, with experimental verifications on the steady-state performance, dynamic response, and a start-up procedure.

II. TWO-TERMINAL ACTIVE CAPACITOR CONCEPT

Fig. 1 shows the system diagram of a two-terminal active capacitor. A full-bridge converter is connected in series with a capacitor C_1 . It handles only the ripple voltage and ripple current

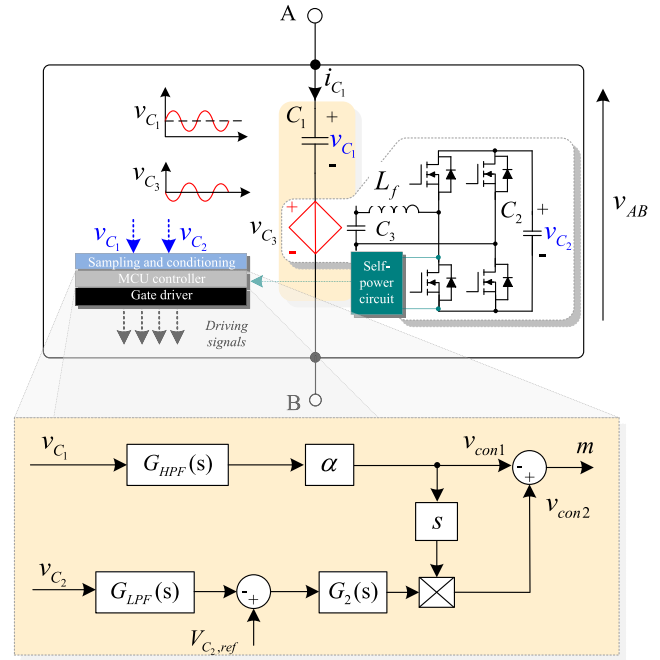


Fig. 1. System diagram of the active capacitor concept presented in [11].

of C_1 , implying a low VA rating. Thus, it is possible to achieve a cost-effective capacitive dc-link solution, as to be discussed in Section III. Moreover, because of the low-rating auxiliary circuit characteristic, specified start-up considerations are needed to guarantee that the electrical stresses of the auxiliary circuit are under rating.

The control objective of the active capacitor is to shape the impedance seen from AB terminals to be that of an equivalent passive capacitor of interest based on internal signals. Therefore, from the control aspect, it enables fully independent operation of the active capacitor without any feedback signals from external circuits. The control method shown in Fig. 1 is to modulate the voltage v_{C_3} to be out of phase with the ripple components in v_{C_1} and same amplitude. $G_{HPF}(s)$, $G_{LPF}(s)$, and $G_2(s)$ are the transfer function of the high-pass filter (HPF), low-pass filter (LPF), and the PI controller, respectively. $V_{C_2,ref}$ is the voltage reference of C_2 , and α is the scaling factor of the ripple component of v_{C_1} . In order to compare the terminal characteristics with the passive capacitor, the impedance characteristics of the active capacitors are derived in Section IV.

III. COMPONENT SIZING OF THE ACTIVE CAPACITOR FOR COST-CONSTRAINT APPLICATIONS

The component sizing of the active capacitor is presented in this section by considering the operating principle, lifetime, and cost. The analytical equations derived in Sections III–V are generic ones, and the presented numerical results in figures are based on a specific design case with specifications described in Table I.

A. Basic Criteria for Component Sizing

1) *Criteria to Size C_1* : C_1 impacts the apparent power handled by the auxiliary circuit and the efficiency.

TABLE I
SPECIFICATION OF THE SINGLE-PHASE SYSTEM WITH AN ACTIVE CAPACITOR

Parameters	Description	Value
P	Power rating	750 W
R_{Load}	Load resistance	53 Ω
v_{AC}	Grid voltage RMS	110 V
f_a	Fundamental frequency	60 Hz
n	Order of harmonic considered	2
V_{AB}	Average terminal voltage v_{AB}	200 V
L_g	Inductance of grid side inductor	0.75 mH
α_v	DC-link voltage ripple ratio	5%
f_{sw}	Switching frequency	20 kHz
$V_{C2,ref}$	Voltage reference of v_{C2}	60 V
C_1	Capacitance of C_1	110 $\mu\text{F}/250\text{ V}$
C_2	Capacitance of C_2	470 $\mu\text{F}/100\text{ V}$
C_3	Capacitance of C_3	3 $\mu\text{F}/63\text{ V}$
L_f	Inductance of L_f	100 $\mu\text{H}/3\text{ A}$
R_1	ESR of the passive capacitor	405 m Ω
R_2	ESR of C_1	4 m Ω

- a) *Constraint I—Apparent power limit of the auxiliary circuit:* In a steady-state operation, the current flowing through the active capacitor $i_{C_1}(t)$ is given by

$$i_{C_1}(t) = \sum I_n \cos(n\omega t + \delta_n) \quad (1)$$

where ω is the fundamental frequency and n is the order of harmonics. For simplicity, only n th-order harmonic is considered in the following analysis. Superposition principle can be applied if two or more harmonic components are considered. I_n is the amplitude of the ripple current, and δ_n is the phase shift of the ripple current. The steady-state voltage of C_1 is

$$v_{C_1}(t) = V_{AB} + \frac{1}{2} \Delta V_{C_1} \sin(n\omega t + \delta_n) \quad (2)$$

where $\Delta V_{C_1} = \frac{2I_n}{n\omega C_1}$ is the peak-to-peak voltage of C_1 and V_{AB} is the average voltage across the terminals A and B. The control target of $v_{C_3}(t)$ is the inverse voltage of ripple component in $v_{C_1}(t)$; therefore, we have

$$\begin{aligned} v_{C_3}(t) &= -\frac{1}{2} \Delta V_{C_1} \sin(n\omega t + \delta_n) \\ &= -\frac{I_n}{n\omega C_1} \sin(n\omega t + \delta_n). \end{aligned} \quad (3)$$

From the above-mentioned equation, it can be seen that C_1 is inversely proportional to the amplitude of $v_{C_3}(t)$, which determines the voltage stress of the auxiliary circuit. The root mean square (rms) voltage and current of the auxiliary circuit are $\frac{\Delta V_{C_1}}{2\sqrt{2}}$ and $\frac{I_n}{\sqrt{2}}$, respectively, while the processed apparent power ratio of the auxiliary circuit S_{aux} to the main system S_{main} can be derived as

$$\frac{S_{aux}}{S_{main}} = \frac{\frac{\Delta V_{C_1}}{2\sqrt{2}} \times \frac{I_n}{\sqrt{2}}}{S_{main}} = \frac{\Delta V_{C_1} I_n}{4S_{main}}. \quad (4)$$

For the specified single-phase design system with specification described in Table I, the terminal rms voltage and current of the active capacitor are V_{AB} and I_n , respectively, while the processed apparent power ratio is

$$\gamma_S = \frac{S_{aux}}{S_{main}} = \frac{\Delta V_{C_1}}{4V_{AB}}. \quad (5)$$

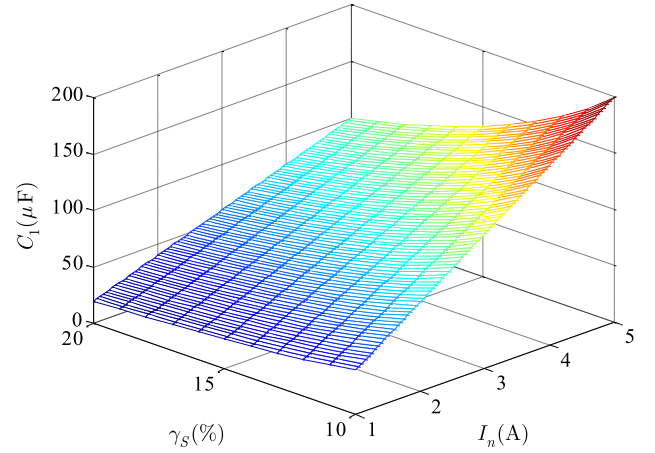


Fig. 2. Relation between C_1 , I_n and ratio of apparent power (for the case study described in Table I).

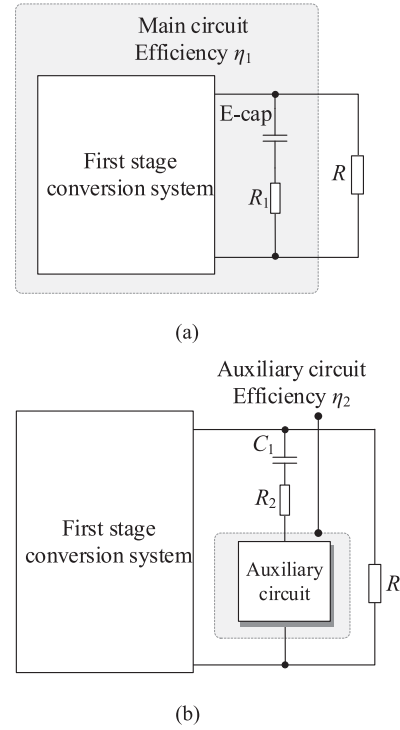


Fig. 3. Diagram of the system with dc-link E-cap and dc-link active capacitor. (a) System with dc-link E-cap. (b) System with dc-link active capacitor.

γ_S implies the apparent power the auxiliary circuit in the active capacitor processed, which affects both the efficiency and the cost of the active capacitor. Substituting $\Delta V_{C_1} = \frac{2I_n}{n\omega C_1}$ into the above-mentioned equation, the value of C_1 should satisfy

$$C_1 \geq \frac{I_n}{2n\omega\gamma_S V_{AB}}. \quad (6)$$

The relation between C_1 , the ratio of apparent power, and the ripple current is shown in Fig. 2.

- b) *Constraint II—System efficiency limit:* Efficiency is one of the design constraints for active capacitor, which depends on the implementation. As shown in Fig. 3, if it is assumed that the efficiency of the main circuit (with conventional

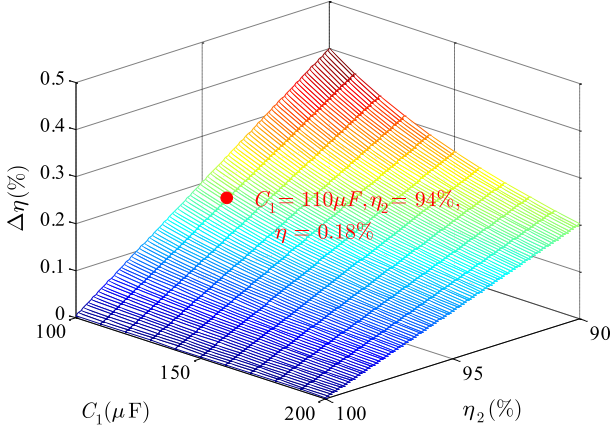


Fig. 4. Relation between efficiency drop $\Delta\eta$ and other design parameters.

passive dc-link capacitor) and auxiliary circuit of the active capacitor can be designed as η_1 and η_2 , respectively, and the ESR of the conventional dc-link capacitor and the capacitor C_1 in the active capacitor are R_1 and R_2 , respectively, the total power loss of the system can be

$$\begin{aligned} P_{\text{loss-total}} &= S_{\text{main}}(1 - \eta_1) - \frac{I_n^2 R_1}{2} \\ &\quad + S_{\text{aux}}(1 - \eta_2) + \frac{I_n^2 R_2}{2} \\ &= S_{\text{main}}(1 - \eta_1) + \frac{\Delta V_{C_1}}{4V_{\text{AB}}} S_{\text{main}}(1 - \eta_2) \\ &\quad - \frac{I_n^2 (R_1 - R_2)}{2}. \end{aligned} \quad (7)$$

Thus, the efficiency of the system with an active capacitor is

$$\begin{aligned} \eta' &= 1 - \frac{P_{\text{loss-total}}}{S_{\text{main}}} = \eta_1 - \frac{\Delta V_{C_1}}{4V_{\text{AB}}}(1 - \eta_2) \\ &\quad + \frac{I_n (R_1 - R_2)}{2V_{\text{AB}}}. \end{aligned} \quad (8)$$

The efficiency drop introduced by the active capacitor can be described by $\Delta\eta$, which is the difference between the efficiency of the system with conventional dc-link E-cap η_1 and the efficiency of the system with an active capacitor η' , and can be written as

$$\begin{aligned} \Delta\eta &= \eta_1 - \eta' = \frac{\Delta V_{C_1}}{4V_{\text{AB}}}(1 - \eta_2) - \frac{I_n (R_1 - R_2)}{2V_{\text{AB}}} \\ &= \frac{I_n}{2V_{\text{AB}}} \left(\frac{1 - \eta_2}{2n\omega C_1} - R_1 + R_2 \right). \end{aligned} \quad (9)$$

With a maximum allowable efficiency drop, $\Delta\eta_{\text{max}}$ is defined, the value of C_1 should satisfy

$$C_1 \geq \frac{I_n - I_n \eta_2}{4n\omega V_{\text{AB}} \Delta\eta_{\text{max}} - 2nR_2 I_n \omega + 2nR_1 I_n \omega}. \quad (10)$$

The relationship between C_1 , η_2 , and $\Delta\eta$ is shown in Fig. 4, where $R_1 = 405 \text{ m}\Omega$ and $R_2 = 10 \text{ m}\Omega$ are measured by the impedance analyzer Agilent E4980A. If η_2

is 94%, the efficiency drop is 0.18%. The capacitance of C_1 also affects the efficiency drop of the system. With larger C_1 , the efficiency drop is smaller because the power handled by the auxiliary circuit is reduced.

2) *Criteria to Size C_2* : C_2 is the dc-link capacitor of the auxiliary circuit in the active capacitor. The capacitance of C_2 has impact on the operation of the auxiliary circuit. Two constraints that need to be considered to size C_2 are as follows.

a) *Constraint I—Voltage controllability*: Based on the control scheme shown in Fig. 1, the relation between $v_{C_3}(t)$ and $v_{C_2}(t)$ is expressed as

$$v_{C_3}(t) = m(t)v_{C_2}(t) \quad (11)$$

where $m(t)$ is the modulation signal; it depends on the following two control signals.

1) $v_{\text{con1}}(t)$ —the extracted ripple component of $v_{C_1}(t)$ used to control the converter to generate the desired $v_{C_3}(t)$.

2) $v_{\text{con2}}(t)$ is used to stabilize $v_{C_2}(t)$.

Moreover, the phase of v_{con2} and i_{C_1} is synchronized (i.e., a 90° phase shift with v_{con1}) in order to absorb active power from external circuits through terminals A and B shown in Fig. 1 to compensate the power loss of the auxiliary circuit. Therefore, we have

$$m(t) = \frac{v_{\text{con1}}(t) + v_{\text{con2}}(t)}{V_{\text{tric}}} \quad (12)$$

where $v_{\text{con1}}(t) = -\frac{1}{2}\alpha\Delta V_{C_1} \sin(n\omega t + \delta_n)$. V_{tric} is the amplitude of the triangular carrier wave. The current of C_2 can be obtained from

$$i_{C_2}(t) = m(t)[i_{C_1}(t) - i_{C_3}(t)]. \quad (13)$$

By ignoring the power loss of the auxiliary circuit, based on (3), (11), and (12), the voltage ripple across C_2 is derived as

$$\begin{aligned} v_{C_2, \text{ripple}}(t) &= \frac{1}{C_2} \int i_{C_2}(t) dt \\ &= \frac{\alpha(C_1 + C_3)I_n^2 [1 + \cos(2n\omega + 2\delta_n)]}{4n^2 \omega^2 C_1^2 C_2 V_{\text{tric}}}. \end{aligned} \quad (14)$$

The peak-to-peak voltage is

$$\Delta V_{C_2} = \frac{\alpha(C_1 + C_3)I_n^2}{2n^2 \omega^2 C_1^2 C_2 V_{\text{tric}}} \quad (15)$$

with the modulation index no more than 1, in order to control the auxiliary circuit

$$v_{C_2}(t) \geq v_{C_3}(t). \quad (16)$$

For the sake of simplification, the minimum value of $v_{C_2}(t)$ is considered as

$$V_{C_2} - \frac{1}{2}\Delta V_{C_2} \geq v_{C_3}(t). \quad (17)$$

Therefore, the value of C_2 should satisfy

$$C_2 \geq \frac{\alpha I_n^2 (C_1 + C_3)}{4n\omega C_1 V_{\text{tric}} (n\omega C_1 V_{C_2} - I_n)}. \quad (18)$$

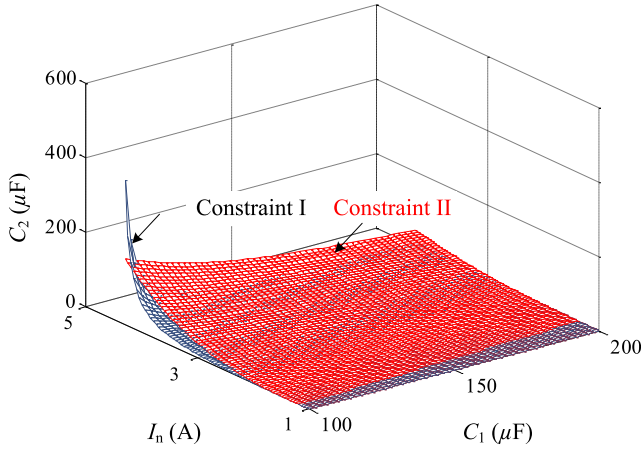


Fig. 5. Component sizing constraints of C_2 .

- b) *Constraint II—Voltage ripple limitation of v_{AB}* : The sizing of C_2 should also consider the voltage ripple limitation of v_{AB} defined in Fig. 1. Voltage variations of C_2 introduce ripple to v_{C_3} and therefore the voltage across the terminals A and B. The relationship is described as

$$v_{C_3}(t) = m(t)v_{C_2}(t) = \frac{v_{\text{con1}}(t)}{V_{\text{tric}}}V_{C_2} + \frac{v_{\text{con2}}(t)}{V_{\text{tric}}}V_{C_2} + \frac{v_{\text{con1}}(t) + v_{\text{con2}}(t)}{V_{\text{tric}}}v_{C_2,\text{ripple}}(t). \quad (19)$$

The first part of (19) is the expected component of $v_{C_3}(t)$, the second part is used for compensating the power loss, and the third part is additional voltage ripples introduced by $v_{\text{con2}}(t)$ and $v_{C_2,\text{ripple}}(t)$. By ignoring the power loss effect of the auxiliary circuit, the third part of voltage ripple also appears at the two terminals A and B, which should be limited to its voltage specification of v_{AB} as

$$\begin{aligned} v_{C_3,\text{ripple}}(t) &= v_{C_2,\text{ripple}}(t) \frac{v_{\text{con1}}(t)}{V_{\text{tric}}} \\ &= \frac{\alpha^2 \Delta I_n^3 (C_1 + C_3) \cos^2(n\omega t + \delta) \sin(n\omega t + \delta)}{4n^3 \omega^3 C_1^3 C_2 V_{\text{tric}}^2} \\ &\leq \alpha_v V_{AB} \end{aligned} \quad (20)$$

where α_v is the voltage ripple ratio defined in the system specification. Thus, C_2 should satisfy

$$\begin{aligned} C_2 &\geq \max \left\{ \frac{\alpha^2 I_n^3 (C_1 + C_3) \cos^2(n\omega t + \delta) \sin(n\omega t + \delta)}{4n^3 \omega^3 C_1^3 V_{\text{tric}}^2 \alpha_v V_{AB}} \right\} \\ &= \frac{\alpha^2 I_n^3 (C_1 + C_3)}{6\sqrt{3}n^3 \omega^3 C_1^3 V_{\text{tric}}^2 \alpha_v V_{AB}}. \end{aligned} \quad (21)$$

Fig. 5 shows the two constraint surfaces of size C_2 . The minimum value of C_2 also depends on C_1 and I_n .

B. Component Sizing for the Active Capacitor for Multiple Constraints

For different applications, the design criteria of active capacitor are different from case to case. The design criteria covers the aspects of functionality, efficiency, lifetime, and cost. The weighted importance of each of them would depend on applications. In order to achieve the systems' requirement, a design procedure for an active capacitor with multiple design constraints is presented, as shown in Fig. 6. In this study, the design scenario is to minimize the design cost with specific requirements on the functionality (e.g., capacitor terminal voltage ripple limit, controllability), efficiency, and lifetime.

The inputs of the design procedure are the mission profile and the design constraints for a specified application. Mission profile includes the operating conditions of the active capacitor, such as the ambient temperature and the loading conditions. The design constraints cover aspects of functionality, efficiency, lifetime, and cost. For different mission profile and design constraint, the component sizing results are different. The first step of the design procedure is the component sizing for functionality, due to it being the first priority. C_1 , C_2 , filters, and switches with corresponding rated electrical stress can be obtained according to the sizing criteria discussed in Section III-A. By searching the available devices in the market, the devices that can fulfill the required parameters can be selected. The second step is to evaluate the performance of these components in terms of power loss, cost, and lifetime. For the capacitors, the ripple current and ambient temperature are the contributors to the internal thermal stress. Especially, the increase of the capacitor power loss causes a higher hot-spot temperature. Lifetime prediction for the capacitor is based on the hot-spot temperature and the voltage stress. For the power semiconductor, the power losses consist of the conduction loss and the switching loss, which will induce thermal stresses. Then, the lifetime of the power semiconductors can be obtained by using the lifetime model [29]. For the sake of simplicity, the wear out failure of the switches within the targeted lifetime period is assumed much lower than that of the capacitors if its maximum junction temperature is below 100° [13]. Since it is assumed that the magnetic components usually has less degradation compared to active switches and capacitors, the lifetime aspect analysis of magnetic components is not considered in this paper. The sizing of the inductor is based on achieving the same ripple current ratio. After the summation of component performance, if there is any one aspect that cannot reach the design target, another series components with different parameters will be selected to evaluate the performance.

By changing the parameters of the circuit and the components within the basic criteria discussed in Section III-A, an active capacitor that can achieve multiple design constraints can be selected. Details regarding the lifetime estimation procedure and cost models can be found in [13].

IV. IMPEDANCE CHARACTERISTICS OF THE ACTIVE CAPACITOR

A. Modeling of the Active Capacitor

In order to simplify the analysis, the power converter is assumed to be lossless and the ESRs of the passive components

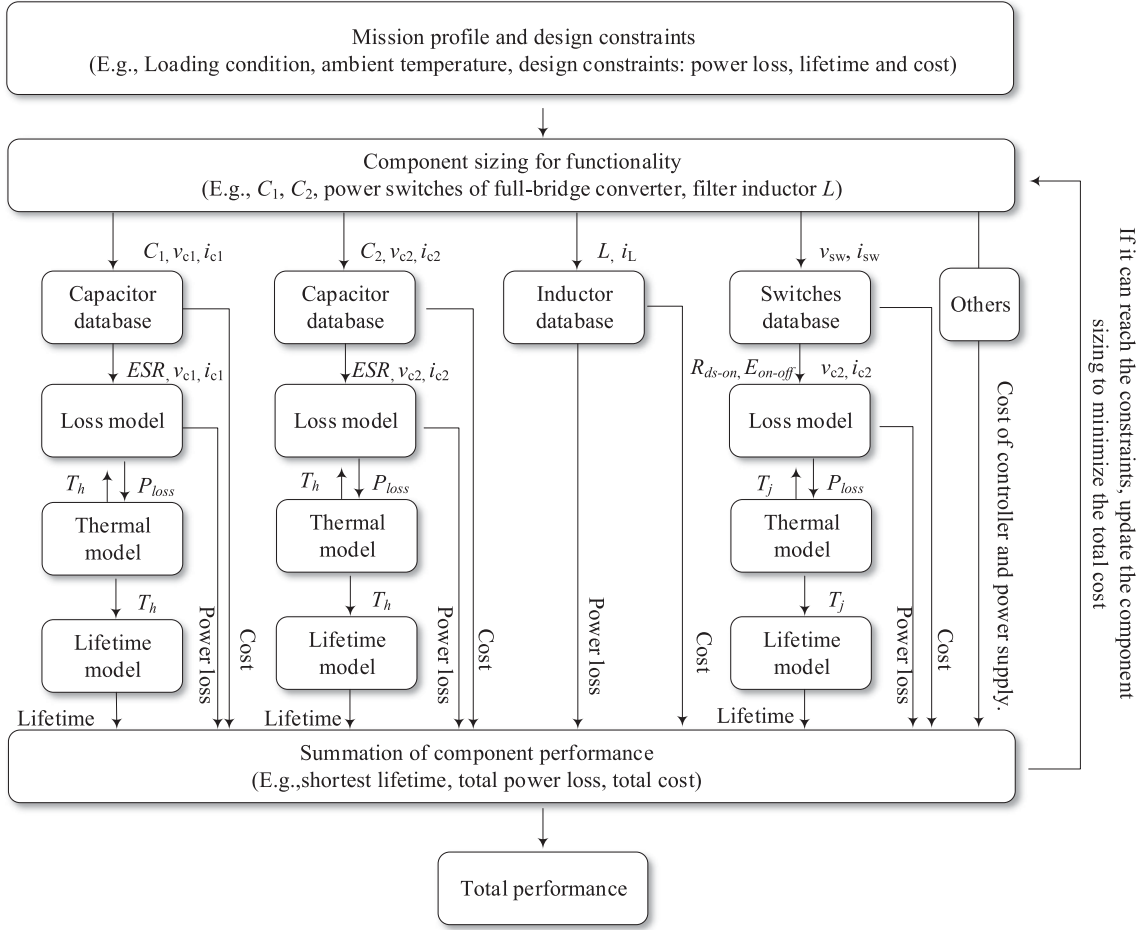


Fig. 6. Flowchart of component sizing procedure considering the reliability and the cost of the active capacitor.

are neglected. The large signal model of the active capacitor is shown as follows by ignoring the high-frequency LC filter for switching harmonics:

$$\begin{cases} C_2 \frac{dv_{C_2}(t)}{dt} = C_1 \frac{dv_{C_1}(t)}{dt} m(t) \\ v_{C_2}(t) m(t) = v_{C_3}(t). \end{cases} \quad (22)$$

By using the averaged ac modeling technique in [30] and neglecting the second-order ac quantities and processing only with the ac equations, the rms-based small signal modeling of the system can be written as

$$\begin{cases} C_2 \tilde{v}_{C_2}(s) s = C_1 \tilde{v}_{C_1}(s) M s \\ \tilde{v}_{C_2}(s) M + \tilde{m}(s) V_{C_2} - \tilde{v}_{C_3}(s) = 0 \end{cases} \quad (23)$$

where $\tilde{v}_{C_1}(s)$, $\tilde{v}_{C_2}(s)$, $\tilde{v}_{C_3}(s)$, and $\tilde{m}(s)$ are the ac perturbations. M is the modulation index. Based on the control structure presented in Fig. 1, it can be seen that the modulation signal contains the following two parts. First, v_{con1} is the extracted ripple component of v_{C_1} used to modulate the converter to generate the desired v_{C_3} . \tilde{v}_{C_1} signal flows through the HPF to extract the ripple component. The ripple is scaled by alpha and reverses as the reference of \tilde{v}_{C_3} . Second, v_{con2} is used to stabilize v_{C_2} . \tilde{v}_{C_2} signal flows through the LPF to extract the dc component. Controller $G_2(s)$ is used to stabilize the voltage of C_2 . $\tilde{m}(s)$ is

calculated as

$$\tilde{m}(s) = \frac{-\alpha G_{HPF}(s) \tilde{v}_{C_1}(s) + G_2(s) G_{LPF}(s) \tilde{v}_{C_2}(s)}{V_{tric}}. \quad (24)$$

The transfer function from $\tilde{v}_{C_1}(s)$ to $\tilde{v}_{C_3}(s)$ can be derived as

$$G_r(s) = \frac{\tilde{v}_{C_3}(s)}{\tilde{v}_{C_1}(s)} = \frac{M C_1 V_{C_2} G_2(s) G_{LPF}(s) + M^2 C_1 V_{tric}}{C_2 V_{tric}} - \frac{\alpha C_2 V_{C_2} G_{HPF}(s)}{C_2 V_{tric}}. \quad (25)$$

The impedance of the active capacitor is obtained as follows and is plotted in Fig. 7:

$$\begin{aligned} Z_{ACap}(s) &= \frac{\tilde{v}_{C_3}(s) + \tilde{v}_{C_1}(s)}{\tilde{i}_{C_1}(s)} = \frac{1 + G_r(s)}{C_1 s} \\ &= \frac{M C_1 V_{C_2} G_2(s) G_{LPF}(s) + M^2 C_1 V_{tric}}{C_1 C_2 V_{tric} s} \\ &\quad - \frac{\alpha C_2 V_{C_2} G_{HPF}(s) + C_2 V_{tric}}{C_1 C_2 V_{tric} s}. \end{aligned} \quad (26)$$

From Fig. 7, it can be seen that the impedance curves of the active capacitor with different HPFs are different, depending on the bandwidth of the HPFs. At a certain low-frequency

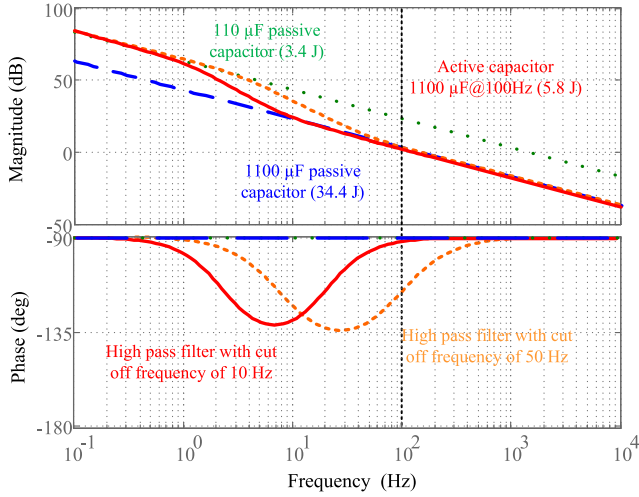


Fig. 7. Impedance comparison between the passive capacitor and active capacitor ignoring the LC filter. The green dot line is the impedance curve of a $110 \mu\text{F}$ passive capacitor with 3.4 J total energy storage; blue dash line is the impedance curve of a $1100 \mu\text{F}$ passive capacitor with 34.3 J total energy storage and red solid line is the impedance curve of the active capacitor with 5.8 J total energy storage. The red and orange curves are the impedance curve of the active capacitor with 10 and 50 Hz HPFs.

bandwidth, the impedance characteristics is same with C_1 . In the middle-frequency bandwidth, the HPF starts to work. The active capacitor has an equivalent negative resistance component at this certain frequency range, which is due to the impact of the introduced HPF $G_{\text{HPF}}(s)$ shown in Fig. 1. It implies that the auxiliary circuit releases power and the capacitor C_2 is discharged if low-frequency disturbances appear (e.g., below 100 Hz when the cutoff frequency of $G_{\text{HPF}}(s)$ is 10 Hz). At the frequency higher than the middle bandwidth, such as $\geq 100 \text{ Hz}$, the HPF operates to extract all the harmonics, while the active capacitor has the same characteristics with the $1100\text{-}\mu\text{F}$ passive capacitor. With a proper selection of the cutoff frequency (e.g., 10 Hz), the phase angle is the same as an ideal capacitor when the frequency is 100 Hz or above, if the power loss is ignored, which is the frequency range of interest for the dc-link current during the steady-state operation. The impedance differences between a low-frequency and high-frequency bandwidth result in over-voltage during the load change condition, because the capacitor charging current contains both dc and ac components during load changing. The large signal modeling of the active capacitor regarding the dc and ac disturbances is shown in Fig. 8. Fig. 8(a) shows the simplified model of the active capacitor with only ripple compensation loop $v_{\text{con}1}$. R_{Load} is the load of the system.

1) *AC Disturbance*: Fig. 8(b) shows the ac disturbance $\Delta i_{C_1,ac}$ perturbs at the input of the active capacitor and transfers to $\Delta v_{C_1,ac}$. Because $\Delta v_{C_1,ac}$ is an ac signal, it can flow through the HPF to extract the ripple component as the reference signal of v_{C_3} . Thus, the disturbance can propagate all the blocks in the

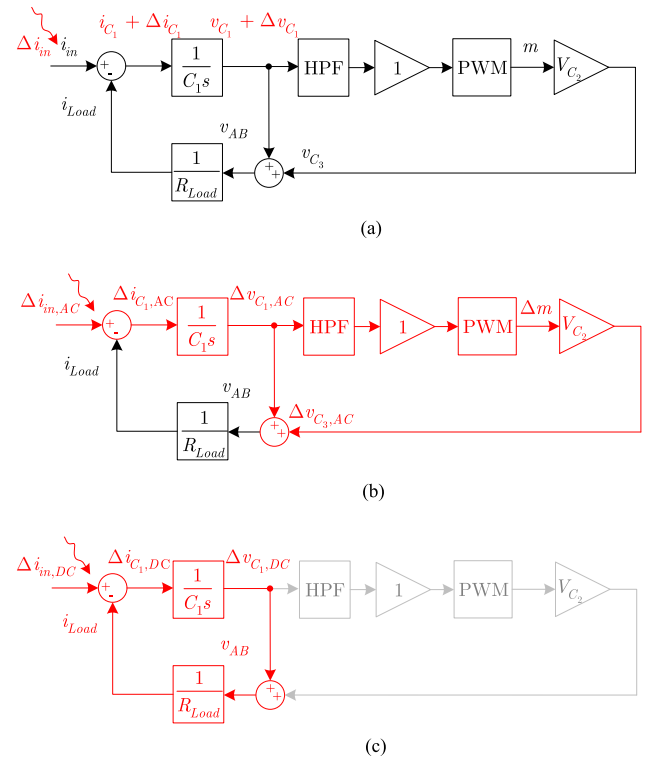


Fig. 8. Equivalent model of the active capacitor for disturbance analysis. (a) Simplified equivalent model of the active capacitor. (b) Flowing path of the ac disturbance. (c) Flowing path of the dc disturbance.

equivalent model with red line. Because of differential compensation between $\Delta v_{C_1,ac}$ and $\Delta v_{C_3,ac}$, there is no disturbance at the AB terminal voltage v_{AB} .

2) *DC Disturbance*: In Fig. 8(c), the dc disturbance $\Delta i_{C_1,dc}$ perturbs at the input and introduce dc voltage on $\Delta v_{C_1,dc}$. Different from the ac disturbance, the dc disturbance $\Delta v_{C_1,dc}$ cannot be filtered by the HPF; therefore, the $\Delta v_{C_3,dc}$ cannot compensate the voltage overshoot or voltage droop of $\Delta v_{C_1,dc}$. The $\Delta v_{C_1,dc}$ disturbance has impact on v_{AB} directly.

From the above-mentioned analysis, it can be seen that the over-voltage during the load change is introduced by the dc disturbance. In order to eliminate the effect introduced by the $\Delta v_{C_1,dc}$, the negative $\Delta v_{C_1,dc}$ is fed at the load disturbance point. The voltage feedforward control scheme is obtained, as shown in Fig. 9(a) and (b). The negative signal is added to the modulation signal for disturbance mitigation. The LPF or notch filter is used to extract the dc component of v_{C_1} , and a saturator is used to obtain the dc disturbance. With this configuration, the controller of the system is nonlinear including two modes. Mode I: Within the bandwidth of the saturator, the feedforward control is disabled. Only the conventional controller is in operation. Mode II: Overtop the bandwidth of the saturator and within modulation capability, the feedforward control is enabled to reduce the over-voltage.

$$C_{\text{eq}}(s) = \frac{C_1 C_2 V_{\text{tric}}}{M C_1 G_2(s) G_{\text{LPF}}(s) V_{C_2} + M^2 C_1 V_{\text{tric}} - \alpha C_2 G_{\text{HPF}}(s) V_{C_2} + C_2 V_{\text{tric}}} \quad (27)$$

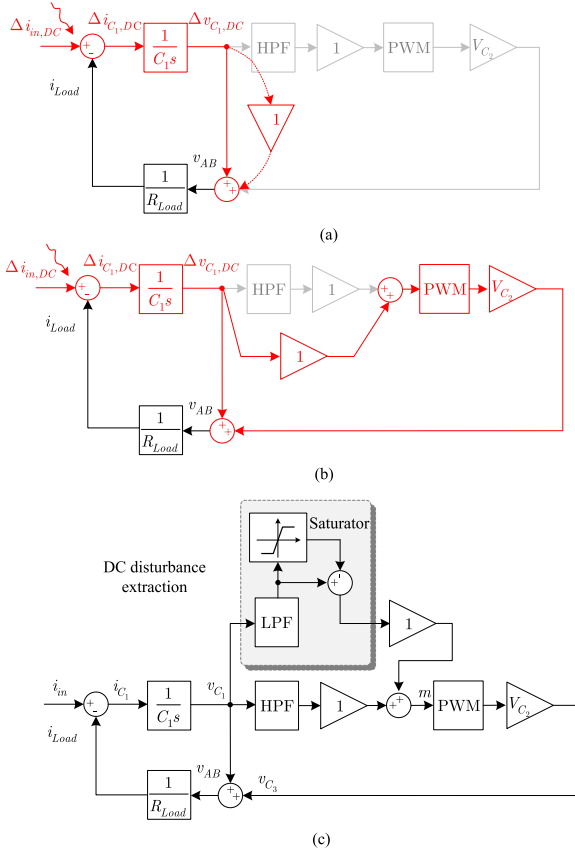


Fig. 9. Derivation of the voltage feedforward compensation scheme for overshoot reduction. (a) Introduction of voltage feedforward. (b) Equivalent transformation of voltage feedforward. (c) Voltage feedforward structure.

B. Equivalent Model of the Active Capacitor

1) *Capacitance*: Based on (26), the equivalent capacitance is obtained as eq.(27) shown at the bottom of previous page, It can be noted that the equivalent capacitance is frequency dependent.

2) *ESR*: The ESR of the active capacitor is derived from the total power loss of the active capacitor contributed by the auxiliary circuit and C_1 . Based on (7), the power loss of the active capacitor is derived as

$$P_{\text{loss-Acap}} = \frac{I_n^2}{2nC_1\omega}(1 - \eta_2) + \frac{I_n^2 R_2}{2}. \quad (28)$$

The equivalent ESR of the active capacitor can be obtained as follows:

$$\text{ESR} = \frac{P_{\text{loss-Acap}}}{I_n^2/2} = \frac{(1 - \eta_2)}{nC_1\omega} + R_2. \quad (29)$$

3) *ESL*: ESL of the active capacitor contains two parts, one is L_{C_1} , which is the ESL of C_1 , and the other one is the parasitic inductance of the auxiliary circuit L_{aux} , depending on the physical layout design of the active capacitor, written as

$$\text{ESL} = L_{C_1} + L_{aux}. \quad (30)$$

Assuming the efficiency of the active capacitor is 94% and L_{aux} is 30 nH, the equivalent model is shown in Fig. 10.

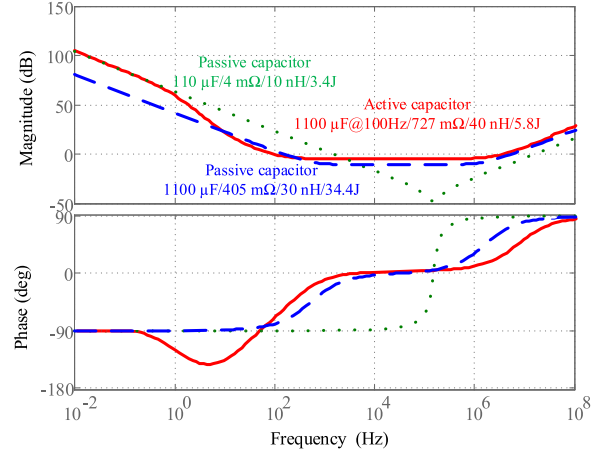


Fig. 10. Bode diagram of the passive capacitor and equivalent Bode diagram of an active capacitor.

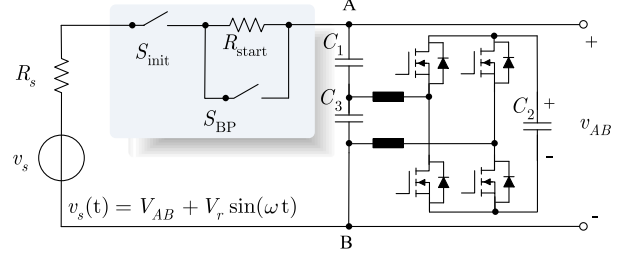


Fig. 11. Circuit diagram of an active capacitor with conventional start-up solution.

In the bandwidth from 100 Hz to 1 kHz of interest, the impedance curves can match with a 1100- μF capacitor with a significantly lower energy storage. The phase angle of the active capacitor at 100 Hz is higher than -90° . It implies that the active capacitor has a positive resistance component and absorbs power from the external circuit through terminals A and B at a higher frequency level (e.g., 100 Hz or above). This mechanism makes it possible to regulate the voltage of capacitor C_2 even under low-frequency disturbances, with the aid of the feedback control loop of v_{C_2} shown in Fig. 1.

V. START-UP SOLUTIONS FOR THE ACTIVE CAPACITOR

This section discusses the start-up process of the active capacitor with a conventional scheme and two proposed solutions to overcome the associated challenge.

A. Start-Up Process Analysis With a Conventional Scheme

Fig. 11 shows a typical start-up circuit widely applied in power electronic circuits [25]. v_s and R_s are the equivalent voltage source and resistor. S_{init} , S_{BP} , and R_{start} are the components of the conventional start-up circuit. If the active capacitor is used in a power electronic system already including such a start-up circuit, the equivalent operation modes of the start-up process are shown in Fig. 12. It assumes that the initial capacitor voltage is 0 V. The three operation modes are described as follows.

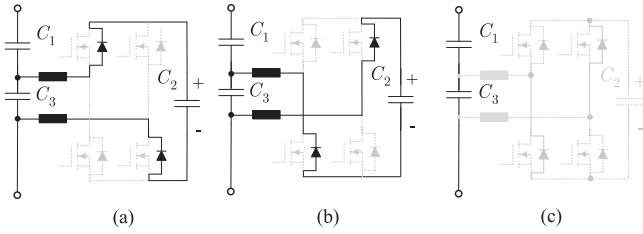


Fig. 12. Three modes of the active capacitor during the start-up procedure. (a) Mode I. (b) Mode II. (c) Mode III.

Mode I: If the voltage of C_3 is higher than voltage of C_2 , C_2 will be charged as shown in Fig. 12(a). It happens at the beginning of several fundamental cycles. The circuit is equivalent to C_2 connected in parallel with C_3 and then connected in series with C_1 . The voltage of C_1 and C_3 can be obtained as

$$\begin{cases} v_{C_1}(t) = (V_{AB} + V_r \sin n\omega t) \frac{C_2 + C_3}{C_1 + C_2 + C_3} \\ v_{C_3}(t) = (V_{AB} + V_r \sin n\omega t) \frac{C_1}{C_1 + C_2 + C_3}. \end{cases} \quad (31)$$

Thus, the maximum voltage of C_3 becomes

$$V_{C_3,\max} = (V_{AB} + V_r) \frac{C_1}{C_1 + C_2 + C_3}. \quad (32)$$

From the analyses of the three operation modes, it can be seen that the voltage stress of C_3 is effected by the parameters of C_1 , C_2 , and C_3 in mode I.

Mode II: If the negative voltage of C_3 is higher than the voltage of C_2 , C_2 will also be charged, as shown Fig. 12(b) mode II. During the start-up procedure, the dc charging current will introduce dc voltages in C_1 , C_2 , and C_3 . Thus, the negative voltage of C_3 is never higher than the voltage of C_2 . Mode II will not happen during the start-up process.

Mode III: The other mode is when the voltage of C_3 is lower than that of C_2 , the current will only flow through C_1 and C_3 . There will be large ripple voltage on C_3 , which is lower than the voltage of C_2 , otherwise mode III will transfer to mode I. Thus, in this case, the maximum voltage of C_2 is same with that in mode I, while the maximum voltage of C_3 is lower than that of C_2 .

From the above-mentioned three modes analysis, the maximum voltage of C_2 , which is same with the maximum voltage of C_3 , is

$$V_{C_3,\max} = (V_{AB} + V_r) \frac{C_1}{C_1 + C_2 + C_3}. \quad (33)$$

With the conventional start-up solution, the inrush charging current can be limited into the specification of the system. However, C_2 and C_3 may experience over-voltage, depending on the voltage of the source and the parameters of the capacitors.

B. Proposed Start-Up Solutions

According to the analysis in Part A, the key issue is how to limit the maximum voltage of C_2 to avoid over-voltage of the components used in the active capacitor. Two start-up solutions to tackle the issue are proposed below.

1) **Solution I—Re-Sizing of C_2 :** The constraints for sizing C_2 shown in Fig. 5 do not take the start-up process into account.

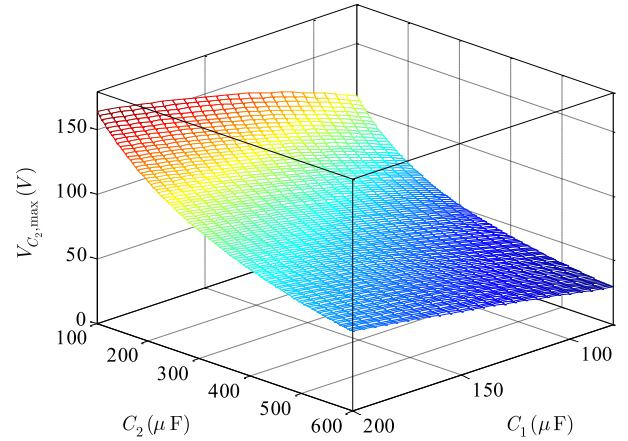


Fig. 13. Relationship between $V_{C_2,\max}$, C_1 , and C_2 for the conventional start-up solution I shown in Fig. 11.

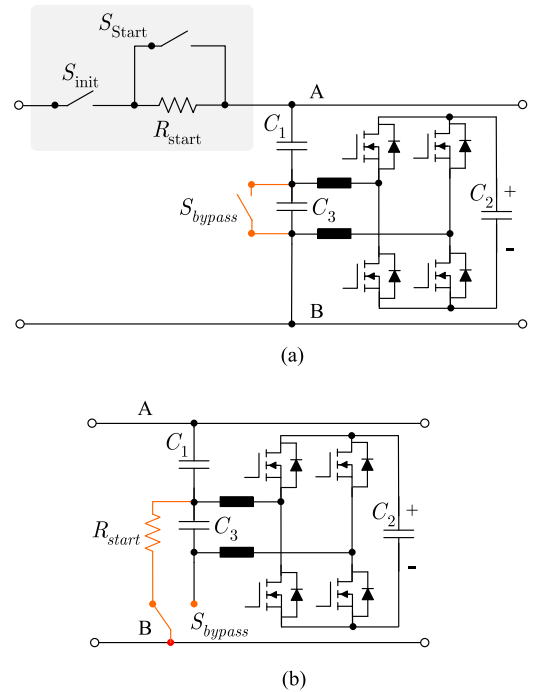


Fig. 14. Startup solution through a bypass switch to charge the C_1 at the beginning. (a) Start-up solution with a bypass switch. (b) Integrated version of the solution shown in Fig. (a).

According to (33), the increase of C_2 is beneficial to the reduction of the maximum voltage of C_2 ; therefore, the voltage stresses on the power switches in the auxiliary circuit of the active capacitor. With the conventional start-up circuit shown in Fig. 11, an additional design constraint among the values of C_1 , C_2 , and maximum voltage of C_2 is obtained, as shown in Fig. 13. For a given limit of $V_{C_2,\max}$ and C_1 , a minimum value of C_2 can be found to avoid over-voltage during the start-up process. The drawback of this solution is that a higher value of C_2 is required compared to that based on the constraints shown in Fig. 5.

2) **Solution II—Bypass Switch:** Fig. 14(a) proposes a solution based on a bypass switch connected in parallel with C_3

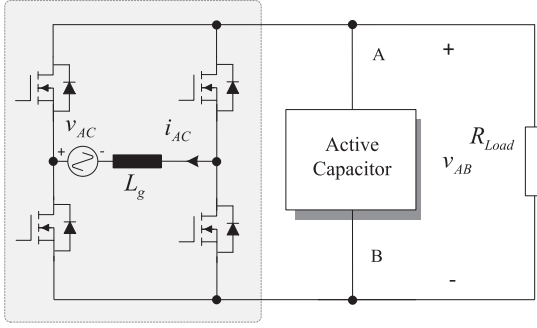


Fig. 15. Circuit topology of the single-phase rectifier with an active capacitor.

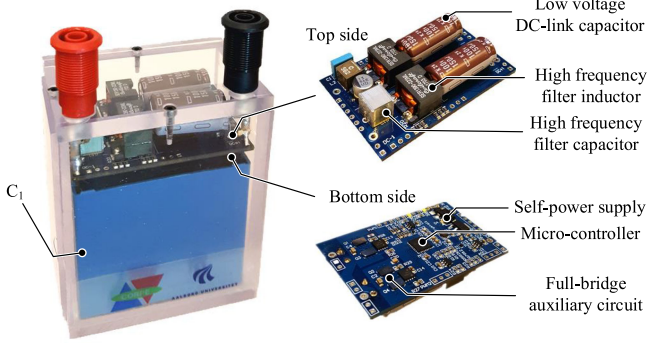


Fig. 16. Two-terminal active capacitor prototype for dc-link application.

without the need of over-sizing C_2 . At the beginning of the startup, the bypass switch S_{bypass} is turned ON. The auxiliary circuit of the active capacitor is bypassed and only the C_1 is charged. Until the voltage of C_1 reaches its steady state, the bypass switch is turned OFF. The capacitors C_2 and C_3 start to be charged.

The charging current and the voltage of C_3 are both sinusoidal, implying that there is no dc voltage in v_{C_3} . The voltage across C_2 finally reaches to the maximum voltage of C_3 , that is

$$V_{C_2, \max} = V_r \frac{C_1}{C_1 + C_2 + C_3}. \quad (34)$$

Fig. 14(b) shows an alternative version of Fig. 14(a) by combing the conventional start-up circuit and the bypass switch function into the active capacitor. The operation principle is similar as the solution shown in Fig. 14(a). The advantage of this integrated version is that the implemented active capacitor has self-start-up protection circuit, which is independent of the external circuit design.

VI. CASE STUDY FOR A CAPACITIVE DC-LINK APPLICATION AND EXPERIMENTAL VERIFICATIONS

This section presents a case study of a two-terminal active capacitor for a capacitive dc link of a 750-W single-phase rectifier, as shown in Fig. 15. The specifications of the rectifier is described in Table I. A two-terminal active capacitor prototype for dc-link application is built up, as shown in Fig. 16. The testing procedure is that run the single-phase rectifier first, while the dc-link active capacitor will be initialized automatically with two start-up solutions. Then, the steady-state and

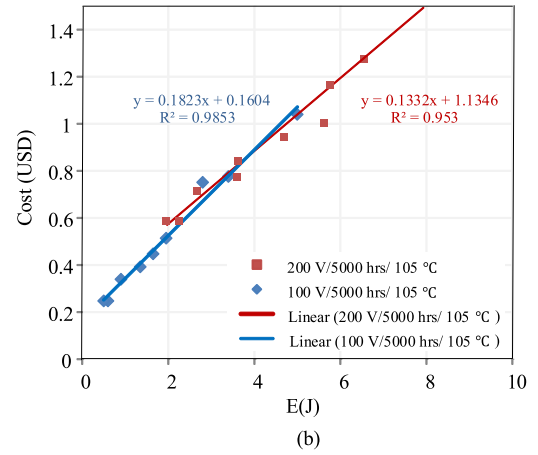
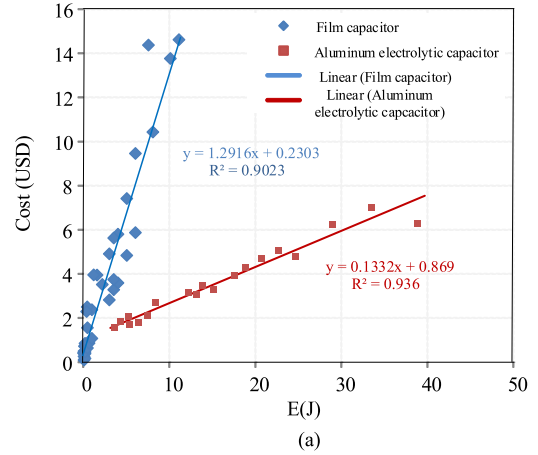


Fig. 17. Capacitor cost model used for sizing C_1 and C_2 [31]. (a) Curve-fitted cost models of 250-V film capacitors and electrolytic capacitors. (b) Curve-fitted cost models of 100-V and 200-V electrolytic capacitors.

dynamic performance of the active capacitor can be provided by changing the load resistance. Following the same testing procedure, the performance of passive capacitor can also be obtained to make a comparable study.

A. Sizing of Key Components for the Cost-Constraint Application

The key components of the two-terminal active capacitors are the capacitors C_1 and C_2 , the four switching devices, the filter inductor L_f , in addition to a small filter capacitor C_3 , the gate drivers and a micro-controller with relatively low computation capability. In principle, C_1 and C_2 can be implemented by electrolytic capacitors, film capacitors, or ceramic capacitors. However, in most practical applications, aluminum electrolytic capacitors may not be suitable for C_1 due to its limited ripple current capability. For high power density applications, ceramic capacitors are preferable to C_1 and C_2 since its high volumetric efficiency as the design demonstrated in [10], at the expense of a relatively high cost. As the presented case study focuses on a cost-constraint application, film capacitors and aluminum electrolytic capacitors are considered for C_1 and C_2 , respectively. It should be noted that even moderate aluminum electrolytic

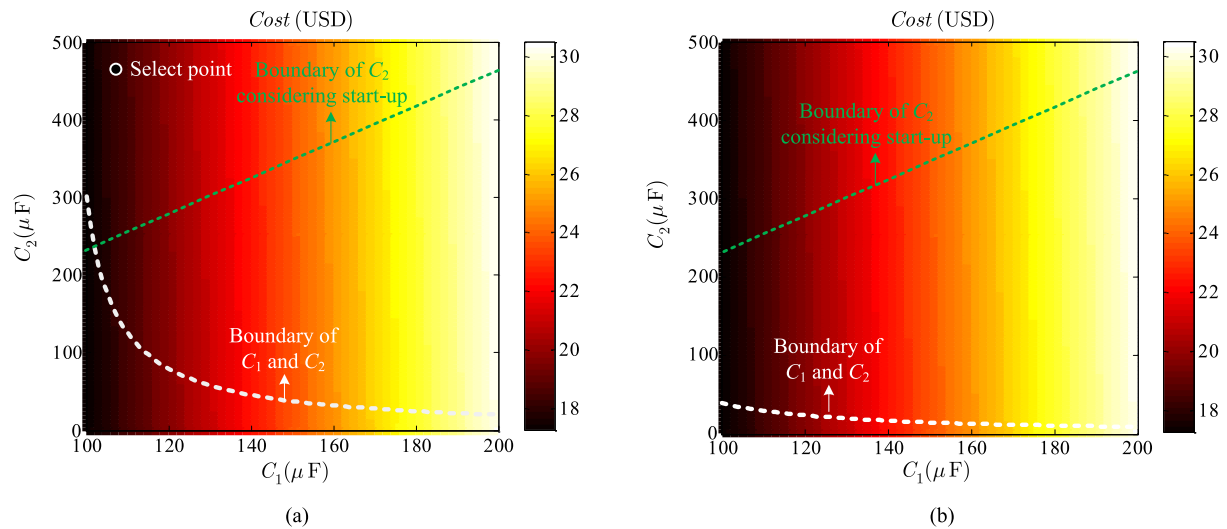


Fig. 18. Relationship between the capacitance of C_1 , C_2 , and the total cost of the active capacitor. (a) Design space of C_1 and C_2 with a mapping of total component cost ($V_{C2,max} = 66$ V, by considering 100 V switching devices with 50% voltage margin). (b) Design space of C_1 and C_2 with a mapping of total component cost ($V_{C2,max} = 100$ V, by considering 150 V switching devices with 50% voltage margin).

TABLE II
COST OF THE AUXILIARY CIRCUIT FOR THE ACTIVE CAPACITOR [31]

Component	Detail information	5 years cost	15 years cost	30 year cost
Passive capacitor	1200/250 V, ELXS251VSN122MA40S	6.4	19.2	38.4
C_1	60 μ F/250 V*2, C4ATDBW5600A30J	16.4	16.4	16.4
C_2	470 μ F/100 V, UVR2A471MHD	0.5	1.5	3
MOSFETs	100 V, IRLR3410TRLPPBF*4	2	2	2
Micro controller	Microchip dsPIC30F2011	2.6	2.6	2.6
Amplifiers IC	TLV2362IDR*2	0.6	0.6	0.6
Power supply	UA78M*2	0.6	0.6	0.6
PCB		1	1	1
Others		1	1	1

capacitors could achieve as long as 15 years of lifetime by thermal and electrical aspects of derating [32]. Therefore, film capacitors are not necessarily favorable for C_2 to meet a specific lifetime target from the cost point of view. In order to establish the relationship between the component costs and the design constraints discussed in Section III, the component cost modeling method presented in [13] is applied to analyze the total component cost. Particularly, the cost models of film capacitors and aluminum electrolytic capacitors are shown in Fig. 17, which is based on the price information from Digikey [31] with an order quantity of 1000 pcs. In the design of the two-terminal active capacitor, start-up solution I (Re-sizing of C_2) is incorporated, so that the cost comparison does not include the start-up circuit. By taking into account also the cost models of other key components as discussed in [33], the design spaces of C_1 and C_2 with 100 and 150 V switching devices (50% voltage margin) are shown in Fig. 17(a) and (b), respectively.

It should be pointed out that the cost mapping shown in Fig. 18 is based on limited component price information and without considering the manufacturing cost and installation cost, etc. The numerical results serve as a comparative study for preliminary selection of design solutions. More comprehensive cost information is needed for a more accurate analysis.

From Fig. 18(a), it can be seen that the cost of the active capacitor is mainly determined by C_1 . The dashed line is the

design constraint of C_1 and C_2 , in consistent with that shown in Fig. 5. Each design point above the dash line may result in a different lifetime as well. The reliability-oriented sizing procedures for the capacitors and switching devices follow the ones discussed in [13]. For a 15 years of lifetime target with reliability of 0.9 (e.g., 15 years of B10 lifetime), the selected design point is $C_1 = 110 \mu$ F, $C_2 = 470 \mu$ F, 100 V MOSFETs, as described in Table I as well. The corresponding total component cost is minimum of 18 USD. With 150 V MOSFETs, the minimum component cost becomes 19 USD according to Fig. 18(b).

For fair comparison between the active capacitor with passive capacitor, the auxiliary component described in Table II (e.g., controller, amplifiers ICs, PCB, etc.) should be taken into account [17], [18]. The cost benchmarking between the passive capacitor and the active capacitor is shown in Fig. 19. The total system cost with active capacitor introduces 36.8% increment than that with the passive capacitor for B10 lifetime 15 years lifetime target, and 28.9% reduction than the passive capacitor for B10 lifetime 30 years lifetime target.

B. Steady-State Performance of the Active Capacitor

An experimental setup is built up to verify the active capacitor with $C_1 = 110 \mu$ F, where the selected design point is shown in Fig. 18(a). In the controller, due to the dc-link ripple harmonics

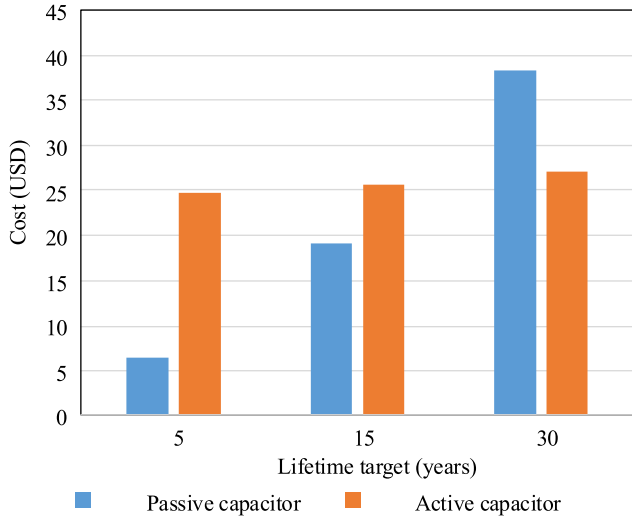


Fig. 19. Cost comparison between the active capacitor and the passive electrolytic capacitor.

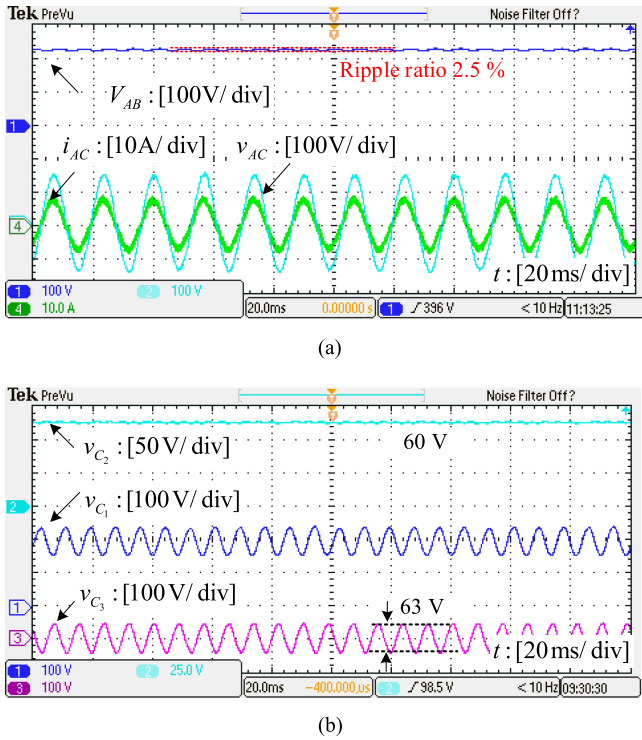


Fig. 20. Steady-state waveforms of the 750-W rectifier with 100% load. (a) Waveforms of the dc-link voltage, and the rectifier input voltage and input current with 50% load. (b) Voltage waveforms of the C_1 , C_2 , and C_3 inside the active capacitor.

is 120 Hz, the cutoff frequency of the HPF is 10 Hz in design. LPF with a 20-Hz cutoff frequency is to acquire dc component of v_{C_2} to maintain a stable dc-link voltage for the full-bridge converter. The PI controller $G_2(s)$ is in the feedback control loop for stabilizing the voltage of C_2 , where the K_p and K_i are tuned as 0.01 and 0.1, respectively. Fig. 20 shows the experimental waveforms of the rectifier and the key components inside the active capacitor under full-load condition. Both ac voltage and current operate with unit power factor, while the voltage ripple

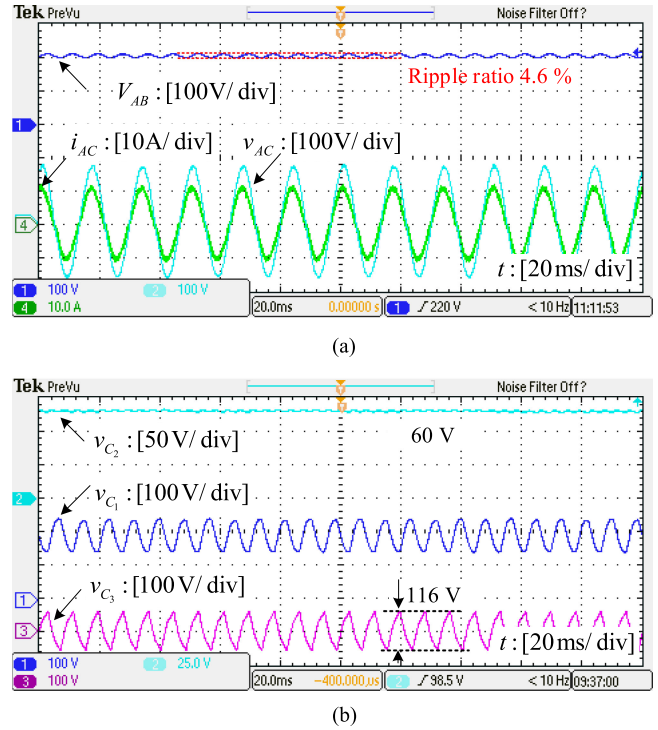


Fig. 21. Steady-state waveforms of the 750-W rectifier with 50% load. (a) Waveforms of the dc-link voltage, and the rectifier input voltage and input current with 100% load. (b) Voltage waveforms of the C_1 , C_2 , and C_3 inside the active capacitor.

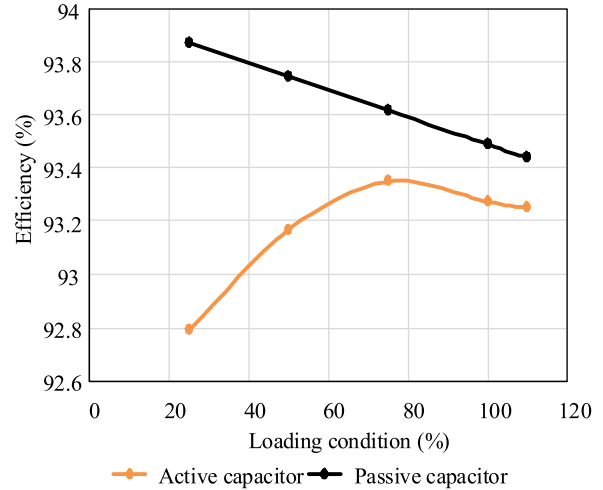


Fig. 22. Efficiency curves of the single-phase systems with active and passive capacitor.

of the dc link is 4.6%, which fulfills the design specification. The average voltage of v_{C_2} is controlled to be constant and v_{C_3} follows the voltage ripple of v_{C_1} . The voltage of C_2 is controlled at 60 V with a ripple of 3.6 V, which is higher than $v_{C_3}(t)$. It can be noted that the voltage ripple of C_1 is approximately out of phase with v_{C_3} . The slight phase shift is due to the mechanism to absorb an insignificant amount of active power to compensate the power loss of the active capacitor. The experimental results with 50% load is shown in Fig. 21. Fig. 22 shows the efficiency of the single-phase system with the active capacitor and the

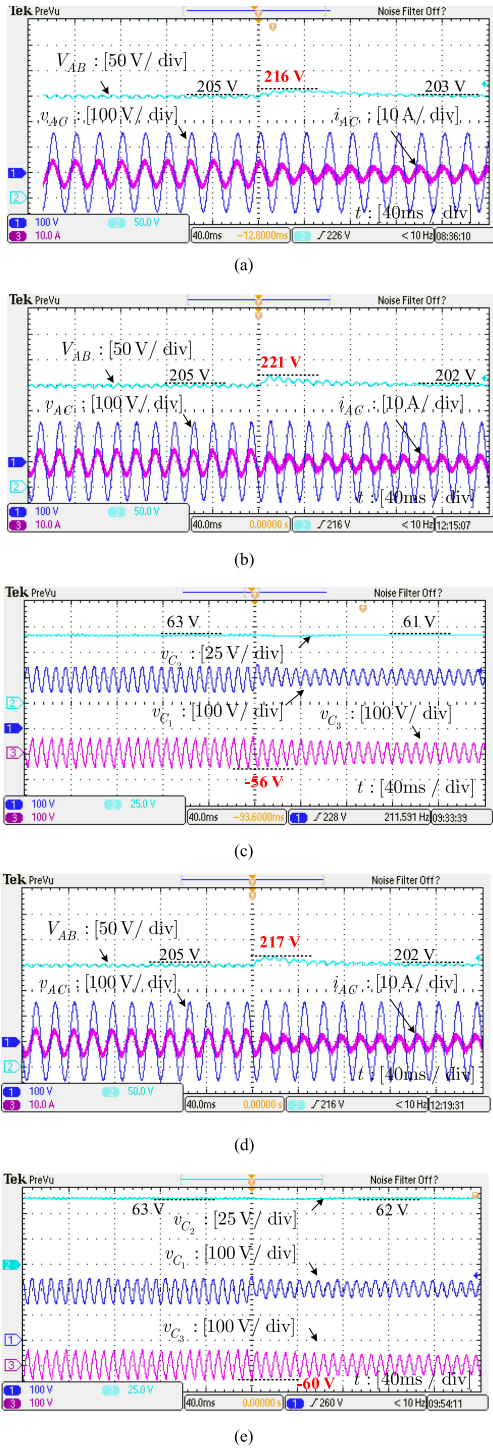


Fig. 23. Experimental waveforms on the dynamic response of a capacitive dc link with a passive capacitor, an active capacitor with and without voltage feedforward control (with a load change from 100% to 50% in a 750-W single-phase rectifier). (a) Dynamic response of a capacitive dc link with a 1100 μF electrolytic capacitor (34.4 J total rated energy storage). (b) Dynamic response of a capacitive dc link with the active capacitor (5.8 J total rated energy storage) without the voltage feedforward control. (c) Dynamic response of voltages of C_1 , C_2 , and C_3 inside the active capacitor (5.8 J total rated energy storage) without the voltage feedforward control. (d) Dynamic response of a capacitive dc link with the active capacitor (5.8 J total rated energy storage) with the voltage feedforward control. (e) Dynamic response of voltages of C_1 , C_2 , and C_3 inside the active capacitor (5.8 J total rated energy storage) with the voltage feedforward control.

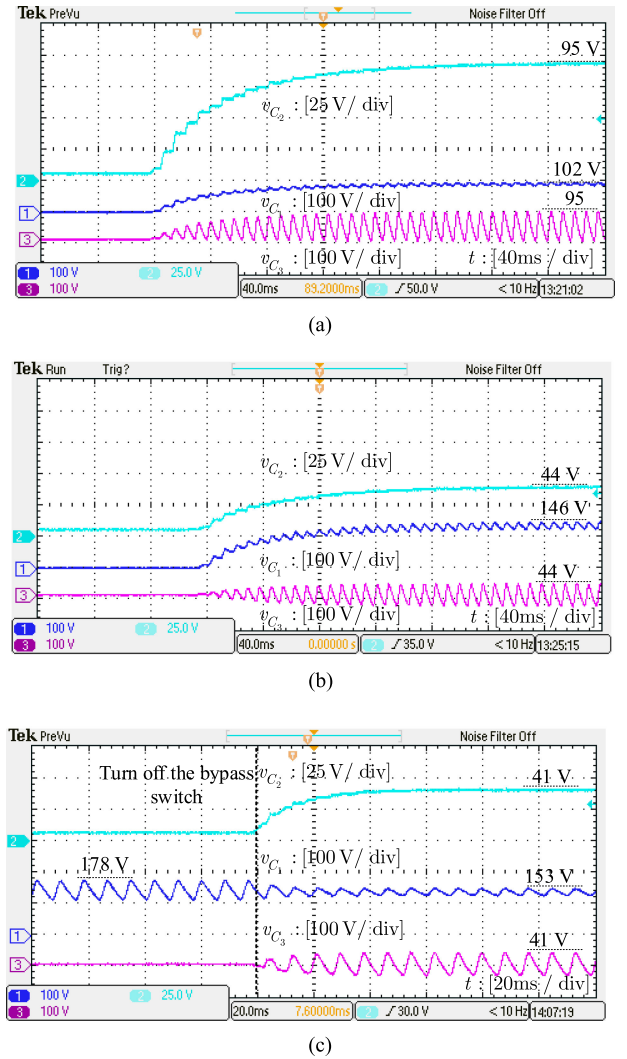


Fig. 24. Experimental waveforms of the voltage stresses of C_1 , C_2 , and C_3 with different start-up solutions. (a) Capacitor waveforms of the active capacitor with conventional start-up solution. (b) Capacitor waveforms of the active capacitor with component sizing solution. (c) Capacitor waveforms of the active capacitor with bypass switch solution.

passive capacitor. With higher power rating, the efficiency of the system with a passive dc-link capacitor is reduced, while the efficiency of the system with the active capacitor is increased. At rated load, the efficiency of the auxiliary circuit is 94%, while the efficiency drop of the whole system introduced by the active capacitor is 0.2%, which is compatible with the analysis in theory.

C. Dynamic Response of the Active Capacitor

The load step-down from 100%–50% is considered as a case study to show the dynamic response of the active capacitor with and without the voltage feedforward control scheme. Fig. 23(a) shows the comparative results of the rectifier with a passive capacitor of 1100 μF (i.e., total rated energy storage of 34.4 J). The dc-link voltage ripples before and after the load change are 5% and 3%, respectively, with an overshoot of 216 V. Fig. 23(b)

shows the experimental waveforms of the rectifier with the active capacitor with the feedforward voltage control. The voltage ripple of the dc link is limited within 5% with 16.8% of total rated energy storage compared to the passive solution, with a slightly higher overshoot of 221 V. The experimental results of the active capacitor with the feedforward compensation are shown in Fig. 23(d) and (e). The overshoot is reduced to 217 V.

D. Start-Up of the Active Capacitor

Following the basic operation criteria discussed in Section III, if $C_1 = 110 \mu\text{F}$, the minimum C_2 is $150 \mu\text{F}$. Fig. 24(a) shows the key waveforms of the active capacitor with $C_2 = 150 \mu\text{F}$. The voltage stresses on C_2 and C_3 are 95 V, which exceed the limit of 60 V. By increasing C_2 to $470 \mu\text{F}$, the maximum voltage stresses of C_2 and C_3 are reduced to 44 V, which is within the design specification, as shown in Fig. 24(b). Fig. 24(c) presents the experimental results with a bypass switch shown in Fig. 14(b). In this implementation, bypass switch is a relay with two switching states. When the dc voltage has been built in C_1 , the switch turns OFF to initialize the active capacitor. At the beginning, the bypass switch is in the ON state. C_1 withstands all the dc-link voltage. There is no current flowing through the auxiliary circuit. When the bypass switch is turned OFF, the ac current charges C_2 and C_3 through the diode bridge. Therefore, no dc component appears in v_{C_3} . The maximum voltages of C_2 and C_3 are limited to 41 V, which is within the design specification.

VII. CONCLUSION

This paper investigates the component sizing, impedance characteristics, and start-up solutions of a two-terminal active capacitor for cost-constraint and reliability-specific applications. In the case study of a 750-W single-phase rectifier with a dc-link voltage of 200 V, the active capacitor achieves comparable steady-state performance and dynamic response as a $1100 \mu\text{F}$ passive capacitor, with 16.9% total rated energy storage only. The overall cost of the active capacitor is 136% as the passive capacitor to fulfill a reliability target of 0.9 at 15 years of service. When it comes to a more demanding reliability performance, the active capacitor has the potential to reduce the overall design cost (i.e., estimated 28.9% cost reduction for a reliability target of 0.9 at 30 years of service). Experimental results also demonstrate the effectiveness of the proposed two start-up solutions to avoid over-stress of the key components in the active capacitor.

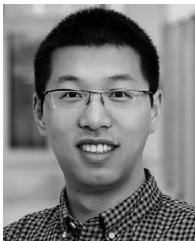
The case study reveals that two-terminal active capacitors become attractive for applications with a relatively high reliability requirement. There are application scenarios that passive capacitor based solutions show superior performance in terms of the design cost. It should be noted that the presented case study is limited to its cope for cost-constraint applications and based on the state-of-the-art reliability modeling and cost modeling approaches. The conclusions drawn from the study are not inclusive to all the application scenarios. With different dc-link voltage levels and dc-link voltage ripple specifications, the application scenarios in which the active capacitors show

better cost-effectiveness can be obtained by following the analysis method proposed in this study.

REFERENCES

- [1] X. Pei, W. Zhou, and Y. Kang, "Analysis and calculation of dc-link current and voltage ripples for three-phase inverter with unbalanced load," *IEEE Trans. Power Electron.*, vol. 30, no. 10, pp. 5401–5412, Oct. 2015.
- [2] M. Liserre, R. Cardenas, M. Molinas, and J. Rodriguez, "Overview of multi-MW wind turbines and wind parks," *IEEE Trans. Ind. Electron.*, vol. 58, no. 4, pp. 1081–1095, Apr. 2011.
- [3] H. Wang and F. Blaabjerg, "Reliability of capacitors for dc-link applications in power electronic converters—an overview," *IEEE Trans. Ind. Appl.*, vol. 50, no. 5, pp. 3569–3578, Sep. 2014.
- [4] Z. Qin, Y. Tang, P. C. Loh, and F. Blaabjerg, "Benchmark of ac and dc active power decoupling circuits for second-order harmonic mitigation in kilowatt-scale single-phase inverters," *IEEE J. Emerg. Sel. Topics Power Electron.*, vol. 4, no. 1, pp. 15–25, Mar. 2016.
- [5] R. Wang *et al.*, "A high power density single-phase PWM rectifier with active ripple energy storage," *IEEE Trans. Power Electron.*, vol. 26, no. 5, pp. 1430–1443, May 2011.
- [6] I. Serban, "Power decoupling method for single-phase h-bridge inverters with no additional power electronics," *IEEE Trans. Ind. Electron.*, vol. 62, no. 8, pp. 4805–4813, Aug. 2015.
- [7] S. Li, G. R. Zhu, S. C. Tan, and S. Y. Hui, "Direct ac/dc rectifier with mitigated low-frequency ripple through inductor-current waveform control," *IEEE Trans. Power Electron.*, vol. 30, no. 8, pp. 4336–4348, Aug. 2015.
- [8] T. Tanaka and S. Funabiki, "A new method of damping harmonic resonance at the dc-link of a large-capacity rectifier-inverter system," in *Proc. IEEE Int. Conf. Power Electron. Drive Syst.*, 1999, vol. 2, pp. 888–893.
- [9] T. Tanaka, S. Fujikawa, and S. Funabiki, "A new method of damping harmonic resonance at the dc link in large-capacity rectifier-inverter systems using a novel regenerating scheme," *IEEE Trans. Ind. Appl.*, vol. 38, no. 4, pp. 1131–1138, Jul. 2002.
- [10] S. Qin, Y. Lei, C. Barth, W. C. Liu, and R. C. N. Pilawa-Podgurski, "A high power density series-stacked energy buffer for power pulsation decoupling in single-phase converters," *IEEE Trans. Power Electron.*, vol. 32, no. 6, pp. 4905–4924, Jun. 2017.
- [11] H. Wang and H. Wang, "A two-terminal active capacitor," *IEEE Trans. Power Electron.*, vol. 32, no. 8, pp. 5893–5896, Aug. 2017.
- [12] H. Wang, "Capacitors in power electronics applications reliability and circuit design, tutorial at IEEE IECON 2016," Oct. 2006. [Online]. Available: http://vbn.aau.dk/files/243654015/IECON_2016_Cap_HW.pdf
- [13] H. Wang, H. Wang, G. Zhu, and F. Blaabjerg, "Cost assessment of three power decoupling methods in a single-phase power converter with a reliability-oriented design procedure," in *Proc. IEEE 8th Int. Power Electron. Motion Control Conf.*, 2016, pp. 3818–3825.
- [14] N. C. Sintamarean, F. Blaabjerg, H. Wang, F. Iannuzzo, and P. de Place Rimmen, "Reliability oriented design tool for the new generation of grid connected PV-inverters," *IEEE Trans. Power Electron.*, vol. 30, no. 5, pp. 2635–2644, May 2015.
- [15] D. Zhou, F. Blaabjerg, T. Franke, M. Tnnes, and M. Lau, "Comparison of wind power converter reliability with low-speed and medium-speed permanent-magnet synchronous generators," *IEEE Trans. Ind. Electron.*, vol. 62, no. 10, pp. 6575–6584, Oct. 2015.
- [16] R. M. Burkart and J. W. Kolar, "Comparative life cycle cost analysis of SI and SIC PV converter systems based on advanced η - ρ - σ multiobjective optimization techniques," *IEEE Trans. Power Electron.*, vol. 32, no. 6, pp. 4344–4358, Jun. 2017.
- [17] G. Domingues-Olavarra, P. Fyhr, A. Reinap, M. Andersson, and M. Alakla, "From chip to converter: A complete cost model for power electronics converters," *IEEE Trans. Power Electron.*, vol. 32, no. 11, pp. 8681–8692, Nov. 2017.
- [18] MOSFET and diode technologies accelerate the global adoption of solar energy.pdf. 2015. [Online]. Available: www.wolfspeed.com/downloads/dl/file/id/557/product/0/sic
- [19] R. W. Erickson and D. Maksimovic, *Fundamentals of Power Electronics*. Norwell, MA, USA: Kluwer, 2001.
- [20] G. Zhu, X. Ruan, L. Zhang, and X. Wang, "On the reduction of second harmonic current and improvement of dynamic response for two-stage single-phase inverter," *IEEE Trans. Power Electron.*, vol. 30, no. 2, pp. 1028–1041, Feb. 2015.

- [21] Y. Yang, X. Ruan, L. Zhang, J. He, and Z. Ye, "Feed-forward scheme for an electrolytic capacitor-less ac/dc led driver to reduce output current ripple," *IEEE Trans. Power Electron.*, vol. 29, no. 10, pp. 5508–5517, Oct. 2014.
- [22] Y. Lei *et al.*, "A 2 kW, single-phase, 7-level, GaN inverter with an active energy buffer achieving 216 w/in³ power density and 97.6% peak efficiency," in *Proc. IEEE Appl. Power Electron. Conf. Expo.*, 2016, pp. 1512–1519.
- [23] VPT, "Application note-inrush current in dc-dc converters," 2017. [Online]. Available: <http://www.vptpower.com/wp-content/uploads/downloads/2017/06/Inrush-current-DC-DC-converters-AN008-1.pdf>
- [24] Amphenol, "Thermometrics product line-ptc thermaistors," 2015. [Online]. Available: <https://www.mouser.com/pdfDocs/AAS-PTC-Thermistors-Training.pdf>
- [25] B. Li *et al.*, "Closed-loop precharge control of modular multilevel converters during start-up processes," *IEEE Trans. Power Electron.*, vol. 30, no. 2, pp. 524–531, Feb. 2015.
- [26] K. Shi, F. Shen, D. Lv, P. Lin, M. Chen, and D. Xu, "A novel start-up scheme for modular multilevel converter," in *Proc. IEEE Energy Convers. Congr. Expo.*, 2012, pp. 4180–4187.
- [27] H. Wang, H. Wang, and M. Lu, "Impedance characteristics modeling of a two-terminal active capacitor," in *Proc. IEEE 18th Workshop Control Modeling Power Electron.*, 2017, pp. 1–7.
- [28] H. Wang and H. Wang, "Reliability-oriented design of a cost-effective active capacitor," in *Proc. IEEE 11th Int. Symp. Diagnostics Elect. Mach., Power Electron. Drives*, 2017, pp. 615–621.
- [29] P. D. Reigosa, H. Wang, Y. Yang, and F. Blaabjerg, "Prediction of bond wire fatigue of IGBTs in a PV inverter under a long-term operation," *IEEE Trans. Power Electron.*, vol. 31, no. 10, pp. 7171–7182, Oct. 2016.
- [30] W. Liu, K. Wang, H. S. Chung, and S. T. Chuang, "Modeling and design of series voltage compensator for reduction of dc-link capacitance in grid-tie solar inverter," *IEEE Trans. Power Electron.*, vol. 30, no. 5, pp. 2534–2548, May 2015.
- [31] 2018. [Online]. Available: <http://www.digikey.com>
- [32] Nippon-Chemi-con, "Aluminum capacitors cataloguetechical note on judicious use of aluminum electrolytic capacitors," 2013. [Online]. Available: <http://www.chemi-con.com/2013AluminumElectrolyticCatalog.pdf>
- [33] R. Burkart and J. W. Kolar, "Component cost models for multi-objective optimizations of switched-mode power converters," in *Proc. IEEE Energy Convers. Congr. Expo.*, 2013, pp. 2139–2146.



Haoran Wang (S'15–M'18) received the B.S. and M.S. degrees in control science and engineering from the Wuhan University of Technology, Wuhan, China, in 2012 and 2015, respectively, and the Ph.D. degree in power electronics from the Department of Energy Technology, Aalborg University, Aalborg, Denmark, in 2018.

He is currently a Postdoctoral Researcher with the Center of Reliable Power Electronics (CORPE), Aalborg University, Aalborg, Denmark. From July 2013 to October 2014, he was a Research Assistant with the Department of Electrical Engineering, Tsinghua University, Beijing, China. He was a Visiting Scientist with the ETH Zurich, Switzerland, from December 2017 to April 2018. His research interests include reliability of power electronics, capacitors in electronic systems, and multiobjective life-cycle performance optimization of power electronic systems.



Yang Liu (M'12–SM'17) was born in Hubei Province, China, in 1979. He received the M.E. and Ph.D. degrees in control science and engineering from the School of Automation, Huazhong University of Science and Technology (HUST), Wuhan, China, in 2005 and 2009, respectively.

He is currently an Associate Professor with the School of Automation, HUST. His research interests include power electronics using SiC and GaN, high performance ac motor drives, and active harmony filter topology and control.



Huai Wang (M'12–SM'17) received the B.E. degree in electrical engineering from the Huazhong University of Science and Technology, Wuhan, China, in 2007, and the Ph.D. degree in power electronics from the City University of Hong Kong, Hong Kong, in 2012.

He is currently an Associate Professor with the Center of Reliable Power Electronics (CORPE), Aalborg University, Aalborg, Denmark. He was a Visiting Scientist with the ETH Zurich, Switzerland, from August to September 2014, and with the Massachusetts Institute of Technology (MIT), USA, from September to November 2013. He was with the ABB Corporate Research Center, Switzerland, in 2009. His research addresses the fundamental challenges in modeling and validation of power electronic component failure mechanisms, and application issues in system-level predictability, condition monitoring, circuit architecture, and robustness design.

Dr. Wang was the recipient of the Richard M. Bass Outstanding Young Power Electronics Engineer Award from the IEEE Power Electronics Society, in 2016, and the Green Talents Award from the German Federal Ministry of Education and Research, in 2014. He is currently the Award Chair of the Technical Committee of the High Performance and Emerging Technologies, IEEE Power Electronics Society, and the Chair of IEEE PELS/IAS/IE Chapter in Denmark. He serves as an Associate Editor for *IET Power Electronics*, the *IEEE JOURNAL OF EMERGING AND SELECTED TOPICS IN POWER ELECTRONICS*, and the *IEEE TRANSACTIONS ON POWER ELECTRONICS*.